

Integrating *in situ* Shear Rheology with Neutron Reflectometry for Structural and Dynamic Analysis of Interfacial Systems

P. Sanchez-Puga,^{1, a)} J. Carrascosa-Tejedor,¹ K.C. Batchu,¹ J. Tajuelo,² M.A. Rubio,³ P. Gutfreund,¹ and A. Maestro⁴

¹⁾ *Institut Laue-Langevin, 38042, Grenoble (France)*

²⁾ *Departamento de Física Interdisciplinar, Facultad de Ciencias, Universidad Nacional de Educación a Distancia (UNED), 28232, Las Rozas (Spain)*

³⁾ *Departamento de Física Fundamental, Facultad de Ciencias, Universidad Nacional de Educación a Distancia (UNED), 28232, Las Rozas (Spain)*

⁴⁾ *Centro de Física de Materiales (CSIC, UPV/EHU)-Materials Physics Center MPC, Paseo Manuel de Lardizabal 5, 20018, San Sebastián, Spain*

(Dated: 8 November 2024)

The study of the structure and mechanical properties of complex fluid interfaces has gained increasing interest in recent decades as a result of its significant scientific relevance to the understanding of biological systems, drug development, and industrial applications. The *in situ* combination of molecular-level structural measurements with the assessment of dynamical (rheological) properties is particularly valuable, as comparing measurements conducted on separate samples under challenging-to-reproduce experimental conditions can be problematic. In this work, we present a new sample environment at the FIGARO instrument, the horizontal neutron reflectometer at the Institut Laue-Langevin, which includes an interfacial shear rheometer operating in the Double Wall-Ring (DWR) geometry, compatible with commercial rotational rheometers. This innovative setup enables simultaneous structural (neutron reflectometry) and dynamical (shear interfacial rheology) measurements on the same sample.

I. INTRODUCTION

Fluid interfaces are found in living systems and in a variety of technological processes. Currently, this significant scientific effort is aimed at exploring the potential of supramolecular assemblies composed of large multifunctional colloidal nanoobjects, encompassing amphiphilic molecules, macromolecules, polymers, and organic and metallic nanoparticles. These interfaces often exhibit complex structural organization, displaying a non-linear response to mechanical deformations¹. The interrelationship between the structural and dynamical characteristics of these complex fluid interfaces is crucial in numerous natural and technological processes. Increasing our knowledge on these phenomena is essential for understanding the fundamentals of various biological processes, the development of new drugs, consumer products, or other industrial applications. Examples of such complex interfaces are the phospholipid bilayer that composes cell membranes together with inclusions of other chemical compounds (cholesterol, proteins, fatty acids, etc.), the pulmonary surfactant, or the tear film. In addition, interfaces are inherent to many products in the food, personal care, and biotherapeutic sectors, where emulsions and foams are ubiquitous.

Several scattering techniques have been developed so far to address interfacial molecular structures². In particular, neutron reflectometry (NR) and X-ray reflectometry (XRR)^{3–5}, together with grazing incidence X-ray diffraction (GIXD)^{6–8}, have been successfully used

to reveal both the in-plane and out-of-plane molecular structure of surface films. XRR offers the advantage of covering a broad range of length scales, enabling high-resolution measurements, while GIXD allows the extraction of fine details of the crystallographic morphology at the molecular scale. However, their high energy and electronic interactions can be detrimental to various soft matter systems. In contrast, NR, while not covering the same range of wavelengths as XRR, provides the unique advantage of allowing diverse contrast variations. This is achieved through sample deuteration or the use of mixtures of water and heavy water, in case of aqueous solutions, to adjust the system's scattering properties. Furthermore, NR is considerably less harmful compared to XRR, making it more suitable for the study of delicate soft matter samples.

In addition to large-scale facilities, other approaches have been used to characterize the microstructure in the plane of fluid interfaces such as atomic force microscopy (AFM)^{9,10}, ellipsometry^{11,12}, fluorescence microscopy^{13,14} or Brewster angle microscopy (BAM)^{15–17} that are of great interest as complementary measures to observe the formation of domains above the micron scale.

Regarding interfacial rheology, several instruments have been designed for the study of the dynamical behavior of interfaces. Examples include several Interfacial Shear Rheometers (ISRs) such as the magnetic needle ISR^{18–20}, the microbutton²¹, and specially designed fixtures for commercial rotational rheometers like the conical bob^{22–24} and Double Wall-Ring (DWR)²⁵. We remark that unless the interfacial flow is largely dominated by the interfacial drag on the probe, a circumstance that

^{a)} Electronic mail: sanchez-puga@ill.fr.

cannot be known a priori, the analysis of the rheological data must be analyzed through flow field-based data analysis (FFBDA hereafter) schemes^{19,20,23,25–28} to properly account for subphase inertia and drag, and to adequately separate elastic and viscous contributions of the interface’s response.

Within this framework, no approach currently exists to simultaneously measure interfacial rheology alongside structure, despite the fact that the high sensitivity of interfacial systems to temperature, evaporation, and other experimental conditions makes it challenging to rigorously compare structural and rheological measurements performed on separate samples. In this work, we present an experimental setup that allows the integration of a highly sensitive interfacial shear rheometry system for *in situ* measurements in the FIGARO²⁹ horizontal reflectometer of the ILL, that is now available as an integrated sample environment for the interfacial science community. To our knowledge, there is no neutron or synchrotron facility worldwide that offers as a standard feature the possibility of making simultaneous structural and high-sensitivity dynamical measurements on the same fluid-fluid interface sample.

This paper is organized as follows: Section I provides a description of the DWR design and data acquisition methodology, while Section II focuses on the device’s performance, including experimental validation using a 1,2-dipalmitoyl-sn-glycero-3-phosphocholine (DPPC) monolayer at the air/water interface, whose structure and dynamical behavior have been previously reported in separate experiments.

II. DESIGN, OPERATION, AND DATA ANALYSIS

A. Experimental setup

Langmuir trough and support system. The mechanical setup designed for the FIGARO beamline at ILL, as shown in Figure 1, includes a custom-designed Langmuir trough featuring a single moving barrier, which has been integrated with a commercial Anton Paar MCR702e Space rheometer through an auxiliary support table system. This trough, fabricated from PTFE and mounted on an aluminum plate, incorporates a copper tube circuit at its base that can be connected to a thermostatic bath, ensuring accurate temperature regulation of the sample.

The mobile barrier, made in POM, traverses the Langmuir trough’s top via a carriage mechanism on a rail, driven by a stepper motor attached to a toothed belt. The trough itself measures 101 mm in width, and the barrier’s 450 mm travel range allows for compression ratios slightly above 5. An interfacial pressure sensor/microbalance (KibronTM) equipped with a 4 mm wide Wilhelmy plate is used for interfacial pressure measurement and control.

The DWR interfacial shear rheometer. The

DWR geometry comprises two main components²⁵: the double wall annular cell that is placed at the Langmuir trough, and the ring probe fixture for the commercial Anton Paar rotational rheometers, available at ILL. The double wall annular cup (see Figure 2), custom made in PTFE, has a double step (inner with radius, $R_i = 20$ mm and outer with radius, $R_o = 28.79$ mm) radial profile to minimize meniscus effects and ensure interface pinning at the edges of the steps. The double wall annular cell is positioned at the trough’s back end, and has two openings, oriented transversely to the barrier motion direction, designed to facilitate a smooth and symmetric entry of interfacial flow into the annular double wall channel. The symmetry axis of the double wall channel is carefully aligned with the rheometer’s probe rotation axis. The geometrical parameters of the double wall and the ring have been selected in order to: i) make the values of the interfacial shear strain at the inner and outer contact lines at the ring surface as close to each other as possible, and ii) make the ring-wall distances (3 mm or more) slightly larger than the air/water capillary length (~ 2.7 mm).

The ring probe has been fabricated using titanium 3D printing technology (3D Systems, Leuven, Belgium), adopting a diamond shaped cross section²⁵ of 1 mm diagonal. The ring probe is not a closed circle but has three small openings, equally spaced in the angular coordinate, to allow for the inner and outer interfacial regions to be at the same interfacial pressure. The ring probe fixture incorporates a specialized top connection that enables seamless, backlash-free integration with disposable system shafts, ensuring compatibility with Anton Paar rheometers available at ILL. Accurate centering of the ring probe in the double wall annular cell is facilitated by the circular shape of the top part of the inner wall section of the shear cell.

Integration with FIGARO. The considerable length of the trough and the specific horizontal and vertical positioning requirements, necessary for it to be properly accommodated on the neutron instrument’s anti-vibration table, demanded the building an auxiliary support table. This support table stands on three legs. The leg placed furthest from the rheometer, rests on an additional plate designed to extend the support surface. This plate effectively enlarges the support area provided by FIGARO’s anti-vibration table, ensuring stable and level placement of the trough during measurements.

The neutron beam incidence area has a footprint on the interface 40 – 60 mm wide and 80 mm long in the directions longitudinal and transversal to the Langmuir trough, respectively. Then the Langmuir trough is placed so that there is a 10 mm gap between the end of the annular shear channel ensemble and the beam footprint, in order to minimize possible meniscus effects. Similar 10 mm gaps were allowed between the neutron beam footprint and the Wilhelmy plate and the mobile barrier at the maximum compression position.

Finally, to ensure optimal control of the experimental

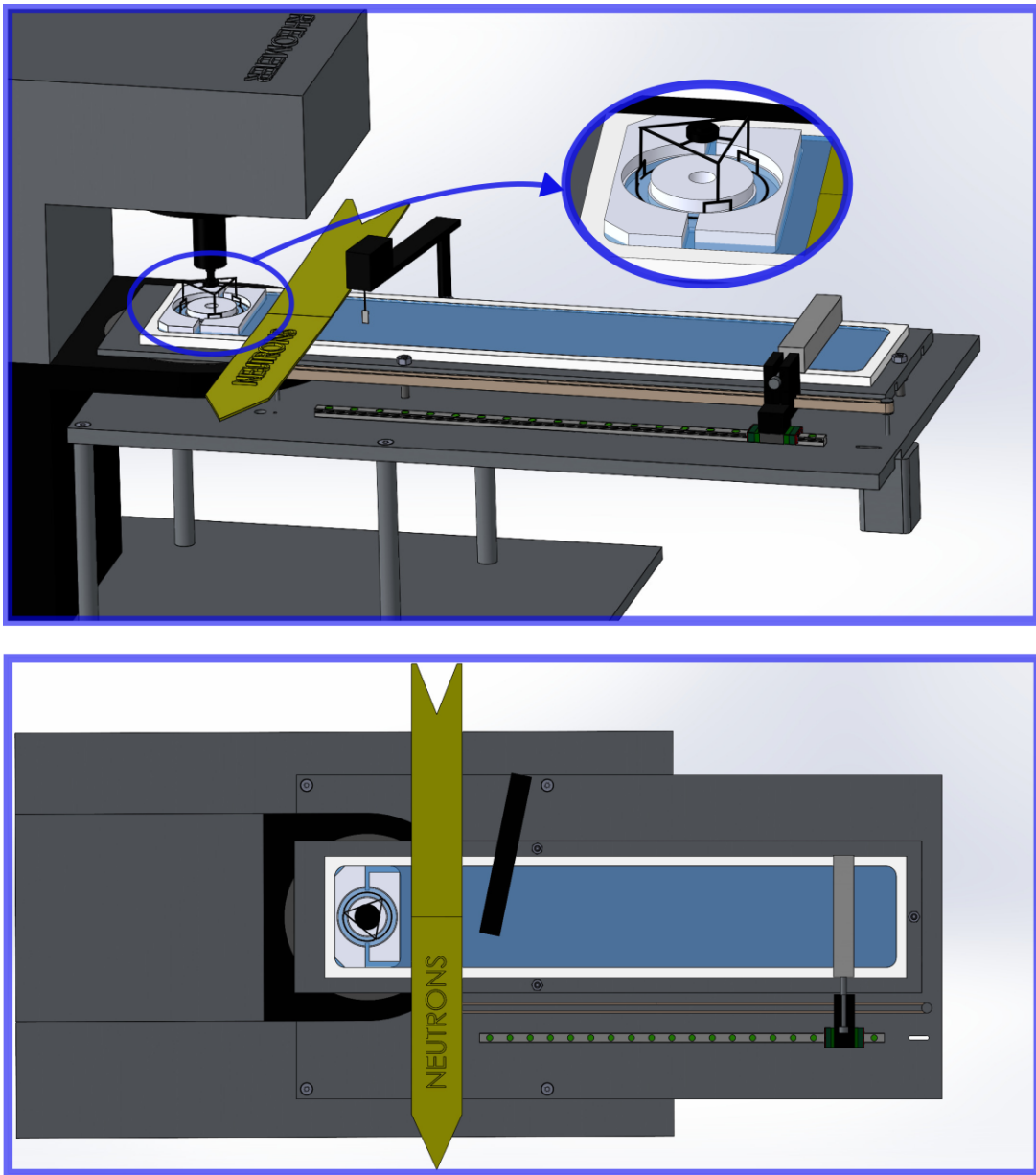


FIG. 1: Sketch of the DWR on FIGARO setup. (a) Top view with a half-height cutting plane showing the disposition of the interfacial rheology measurement system, incident neutron beam and footprint, interfacial pressure balance position, and barrier travel range. (b) Perspective of the whole ensemble attached to the rheometer frame including the support table. (Inset: Detail of the DWR ensemble).

conditions, a cabine has been purposely constructed. The cabine is provided with lateral quartz windows, to facilitate the entry and exit of reflected beams. Moreover, the top wall of the cabine supports a horizontal optical glass window. A laser beam enter the cabine through that window and is used for precise measurement of the vertical distance between the interface and a reference element. This cabine+laser positioning system allows for precise control of the vertical positioning of the interface under study, prevents sample contamination, and enhances the

control over the ambient thermodynamic conditions, basically, air temperature and relative humidity.

B. Electrical connections and data acquisition

In this section we provide an overview of the electrical connection scheme. Figure 3 describes the connections for the interfacial rheology measurement system and the Langmuir trough, which are controlled by the same com-

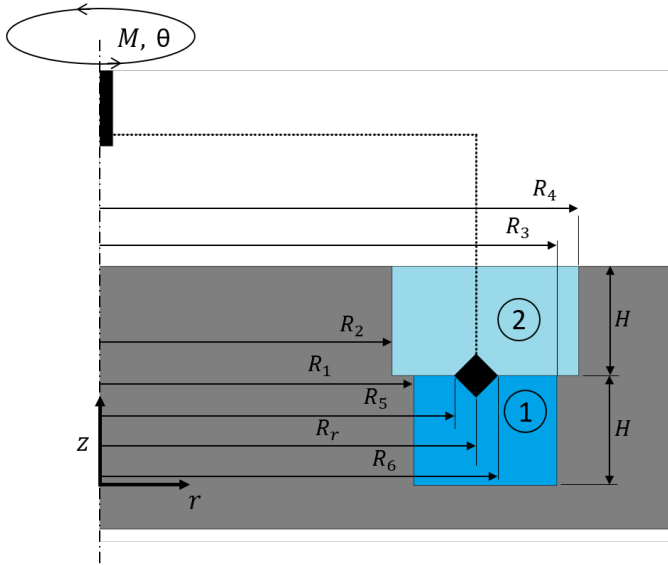


FIG. 2: Sketch of the DWR geometry cross-section (taking advantage of the rotational symmetry, only the right half of the geometry is represented to enhance the details). The different radii are labeled as in reference³⁰.

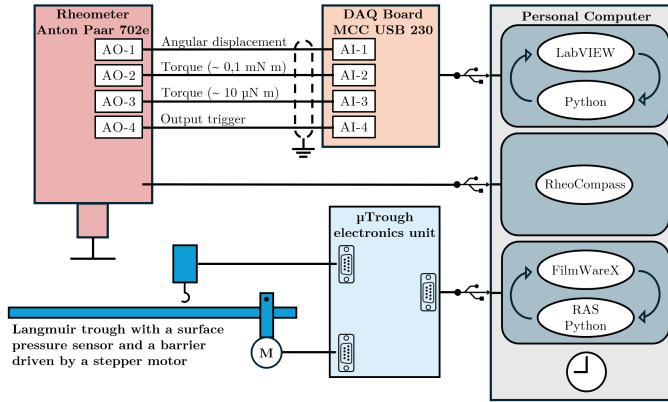


FIG. 3: Sketch of the electrical connections.

puter.

The Anton Paar torsion rheometer here used offers the possibility to configure four analog output signals (± 10 V and 16 bit resolution) with selectable gain values according to user's requirements. In this case, they have been configured to provide the raw signals corresponding to the angular displacement (gain = 600 V/V), the total torque (typically gain = 5×10^5), the total torque (typically gain = 5×10^5), and a trigger signal indicating the start of a new measurement interval of the various measurements that constitute the total experiment. This trigger signal is used to detect the beginning of a new waveform corresponding to a different measurement to be analyzed and stored as raw data for security. These four analogue signals are acquired by means of a USB DAQ board (Digilent MCC USB-234; 8 SE/4 DIFF analog inputs; 16-bit resolution, 100 kS/s maximum sampling fre-

quency,) communication with the control PC by a USB connection. The Anton Paar rheometer is connected by a USB interface to the control tabletop PC where the RheoCompass software that controls all of the functionalities of the rheometer is run. The acquisition and analysis of the raw signals are performed using custom software developed in LabVIEWTM, which integrates Python sub-routines for the more complex calculations.

The electromechanics of the Langmuir trough and the interfacial pressure sensor are connected to a KibronTM μ Trough measurement and control unit that communicates with the control PC by a USB connection. The Kibron proprietary FilmWarex software is mounted in the control PC where it is used to operate the trough. In this case, a Remote Access Server (RAS) has been configured that runs alongside with FilmWareXTM, sharing access to the trough, allowing to communicate and operate the trough by means of string based commands and responses. This centralized single PC control allows to configure our own scripts, in Python to automate experiments and/or perform more complex barrier movement profiles at will.

In this work, the synchronization of rheometry and NR measurements has been achieved by assuring that the time clocks of the rheology and NR systems coincide. In the future, it is planned to integrate Langmuir trough control within NOMAD, a software package developed at ILL, enabling instrument control and data acquisition. This will make possible to trigger rheology measurements from NOMAD or, vice versa, to trigger the NR measurements from the rheometer control software, in case a very precise synchronization is needed. For the experiments performed so far, this level of synchronization has not been necessary.

C. Operation

To operate this experimental setup, four distinct software tools are utilized i) to control the rheometer, ii) to acquire the raw torque and angular displacement signals, iii) to manage the Langmuir trough, and iv) to operate the neutron reflectometer. In the following we will describe some peculiarities of each of these functions

Rheometer control. Exactly positioning the lateral vertices of the ring cross-section at the interface level is crucial in this setup. This task can be splitted in two: i) properly defining the vertical length of the probe fixture and the vertical position of the double wall annular shear channel bottom, using the rheometer's control software (RheoCompassTM) capability of creating user-defined measurement ensembles, and ii) preparing a vertical positioning script that, starting with the ring above the interface, slowly lowers the probe until a jump in the vertical force measurement is detected. Then, the probe is lowered another half a millimeter so that the interface pins on the edge of the diamond-shaped cross-section of the ring. Finally, the vertical force measurement is reset.

A proper configuration of the rheometer control software (RheoCompassTM) for the intended measurements is necessary. Different types of tests can be defined by the user to conduct oscillatory measurements either in single frequency mode, frequency sweep mode, or amplitude sweep mode. The raw torque, angular displacement, and trigger signal are acquired and split into separate waveforms using the trigger signal.

Digitizing the raw rheometry signals. A software package has been programmed in LabVIEWTM that performs the data acquisition, the splitting of the acquired signal into individual waveforms. For each individual waveform, an integer number of periods is selected, discarding the initial part which may contain transients. Then the waveforms are processed by discrete Fourier transforms, to obtain the amplitude and phase of both the torque (T_0 , φ_T) and the angular displacement (θ_0 , φ_θ). From there, the complex amplitude ratio, $AR^* = \frac{T_0}{\theta_0} e^{i(\omega t + (\theta_T - \theta_\varphi))} = |AR^*| e^{i(\omega t + \varphi)}$, is calculated, which serves as input for a purposely built Python program that implements the corresponding FFBDA scheme and is called from LabVIEW, that yields the interfacial dynamic shear moduli by solving the equations governing the velocity field in both the interface and the bulk. These analysis tasks are performed asynchronously in parallel using a queue system as acquisitions are made.

Langmuir trough management. KibronTM components were used in the assembly of the Langmuir trough. Consequently, the Langmuir trough is operated using the company's proprietary software, FilmwareX. This software includes a specialized feature that permits the integration of Python scripts, enabling users to employ various operational modes through the Remote Access Server on a local network. This capability offers significant flexibility, allowing users to automate the measurement process in coordination with neutron scattering data acquisition. Additionally, it facilitates the development of intricate barrier movement profiles, thereby enhancing the precision and complexity of experimental setups.

Operating the neutron reflectometer. The FIGARO instrument at the Institut Laue-Langevin is a high-flux 'time-of-flight' (TOF) reflectometer operated by the NOMAD software. It is equipped with two chopper pairs that allows to select the wavelength resolution. In this study, for instance, it has been used with a constant resolution $d\lambda/\lambda = 7\%$. Three different incidence angles $\theta_1 = 0.62^\circ$, $\theta_2 = 1.97^\circ$, and $\theta_3 = 3.8^\circ$, can be setup. Typically, when seeking a measurement spanning a broad wavelength range, it is preferable to measure at angles θ_1 and θ_2 , because their ranges overlap. Nevertheless, for rapid measurements in studies on kinetic processes³¹, it is feasible to measure at a single incidence angle tailored to the user's wavelength range requirements. Specially noteworthy is the possibility of measuring with high precision the surface excess by measuring at low Q_z (θ_1). This makes possible to quantify the composition of binary mixtures using isotopic contrasts in a suitable manner or in combination with ellipsometry

as a complementary technique. On the other hand, when the objective of the study is to obtain information on the evolution of the interfacial structure, it is possible to perform measurements using higher angles of incidence (θ_2 or θ_3) depending on the range in Q_z where the features of the changes in the reflectivity curve appear. Different isotopic contrasts can be tailored to match the structural complexity of the system under study, and, utilizing deuteration techniques, one can selectively highlight distinct components. The two-dimensional detector signal is processed and reduced using COSMOS³², ultimately yielding the neutron reflectivity, R , with respect to Q_z vector that, considering specular reflection, reads as:

$$Q_z = \frac{4\pi}{\lambda} \sin \theta, \quad (1)$$

where θ is the angle of incidence, and λ is the wavelength. Detailed information can be obtained about layered structures with specular NR. Experimental data are typically analyzed using an optical matrix model that describes neutron reflectivity for layers perpendicular to the interface, each with specific molecular composition and roughness. Parameters such as scattering length density, thickness, solvent volume fraction, and roughness of each layer can be fitted. Constraints can be applied in modeling software to maintain physical accuracy. By using a common model across data with different isotopic contrasts, one can determine the structure and composition of the material at the interface.

III. PERFORMANCE

A. Materials and experimental protocol

The performance of the setup was assessed by measuring DPPC Langmuir monolayers at different interfacial pressures at room temperature (around 22 °C). Chain-deuterated DPPC (d₆₂-DPPC) was received from Avanti Polar Lipids (>99 %). The subphase water, H₂O was obtained through a Milli-Q dispenser (Millipore) and D₂O was used as received from Sigma Aldrich. The Langmuir trough, the annular shear channel, and the lateral barrier were meticulously cleaned using chloroform (Sigma Aldrich). Next, all these components were carefully rinsed with water to eliminate any remaining residues. The DWR probe was submerged in chloroform during about 5 minutes before each experiment for cleaning.

Solutions of lipids in chloroform, at 0.5 mg/mL, were prepared for gentle drop-wise spreading on the interface using a Hamilton micro-syringe until reaching an interfacial pressure of about 2-3 mN/m. The chloroform is then allowed to evaporate and the monolayer to equilibrate for 15 minutes. Then, sequential increments of interfacial pressure, using the constant pressure mode of operation in between steps, allow at each step the acquisition

of full Q_z range NR measurements simultaneously with a set of continuous rheological measurements at a single frequency (3 % strain and 0.5 Hz), followed by measurements during a frequency sweep (0.3 – 3 Hz at 3 % strain) and a strain sweep (1 – 10 % at 0.5 Hz frequency).

Finally, all of the measurements shown in this paper have been performed in strain controlled mode (TruStrainTM) to avoid excessive strains that might extremely shear the sample. However, we point out that in rotational rheometer here used this strain control mode is implemented through a reasonably fast feedback loop that governs the electromechanical torque that is imposed to the probe.

B. Data analysis

Rheology data analysis. In fluid-fluid interfaces, interfacial and bulk phases effects are intrinsically coupled. Hence, the only way to correctly decouple both effects is to work with the flow fields both at the interface and the bulk fluid phases. Obviously this renders the task quite complicated. However, several flow field-based data analysis (FFBDA hereafter) schemes have been proposed recently for different ISR configurations, either in longitudinal^{19,20,26} or rotational motion^{23,25,28}. In all of them, a simple physical model of the flow allows to formulate the Navier-Stokes equations for the bulk fluids flows with just one velocity component (in the DWR the azimuthal one)^{25,27}. Then, the stress balance at the interface is included through the Boussinesq-Scriven equation^{25,26}, considering that only shear stresses occur at the interface and the bulk fluids. The crucial parameter in this problem appears in the Boussinesq-Scriven equation, namely, the complex Boussinesq number, Bq^* that describes the relative importance of interfacial drag compared to bulk drag, and for the most general case of Newtonian bulk fluids and linear viscoelastic interfaces is represented as³³:

$$Bq^* = \frac{\text{surface drag}}{\text{bulk drag}} = \frac{\eta_s^*}{\eta L}, \quad (2)$$

where $\eta_s^* = \eta_s' - i\eta_s''$ is the complex viscosity, η_s' is the actual interfacial shear viscosity, η_s'' represents the interfacial elastic response, and L is a characteristic length scale depending on the geometry (for the DWR on air/water interfaces is typically 0.7 mm). When Bq_s^* is large (say $Bq_s^* \geq 100$) interfacial stresses dominate and simple expressions can be used to obtain the value of Bq_s^* out of the experimental data and, consequently, of η_s^* . Unfortunately, this is not always the case and then it is necessary to properly analyze the data to separate the contributions of the strongly coupled interfacial and bulk flows.

With that ingredients, an iterative procedure is established that involves: 1) solving the Navier-Stokes equations together with the Boussinesq-Scriven equation starting from a *seed* initial value of Bq_s^* , 2) obtaining the values of the interfacial and bulk drags for that flow

configuration, and 3) using the drag values and the experimental value of the complex amplitude ratio, AR^* , to obtain a corrected value for Bq_s^* through and iterative scheme.

Vandebril *et al.*²⁵ first published and made freely available an FFBDA software package (<https://softmat.mat.ethz.ch/opensource.html>) particularly written for the DWR interfacial shear rheometer configurations. In the present case we used to analyze the data a second generation FFBDA software package (freely available too at <https://github.com/psanchez0046/DWR-Drag> that incorporates the following improvements: i) a user selectable increased mesh resolution, ii) a second-order finite differences approximation for drag calculations, and iii) an iterative scheme based on the probe's equation of motion. Full details can be found in³⁰.

It is important to realize that in the DWR configuration the interfacial strain field can be considered uniform only for high values of Bq^* (let's say $Bq^* \geq 100$). For lower values of Bq^* the interfacial strain field is highly nonlinear with the highest strain values just at the probe-interface contact line. After convergence, the FFBDA software package can yield the strain value at the contact line. However, for labeling purposes, in the rest of this report we will use an average strain value, γ_{av} , obtained from the solution of the Boussinesq-Scriven equation in the limit $Bq \rightarrow \infty$, that yields

$$\gamma_{av} = \phi_0 \frac{R_3^2}{R_3^2 - R_6^2} \sim \phi_0 \frac{R_1^2}{R_5^2 - R_1^2} \quad (3)$$

where ϕ_0 is the angular displacement oscillation amplitude and the different radii are as indicated in Figure 2.

NR data. Measured reflectivity curves have been fitted using `refnx`³⁴ software, which allows for interfacial structure modeling in terms of several piled-up layers, and that contains a versatile environment for model refinement and constraint implementation. For instance, in the case of DPPC Langmuir monolayers the interface model can be established straightforward using a macro specific for the modeling of lipid layers (the 'LipidLeaflet' macro). This macro implements the molecular constraint that ensures the same surface excess at both the head-groups layer and the tails layer³⁴⁻³⁶. After the fitting procedure one can obtain the SLD profile across the vertical coordinate and the values of the corresponding parameters defining the transversal structure of the interfacial film. In the data presented here only the chain thickness and the area per molecule have been left as a free parameters in the fitting process (see Table I).

C. Experimental validation of instrument performance

Simultaneous neutron reflectometry and interfacial shear rheology measurements on DPPC monolayers at constant interfacial pressure were carried out to test the performance of the experimental setup. DPPC is one

of the most studied phospholipids, so there is an extensive literature on both neutron reflectivity³⁶ and interfacial rheology^{37,38} that allows us to check the precision of the measurements. Deuterated DPPC was used, with both Air Contrast Matched Water (ACMW, a mixture of D₂O and H₂O leading to a SLD = 0 matching the air layer), and pure D₂O subphases. Measurements have been made at relatively high interfacial pressures (25, 35 and 45 mN/m) away from the LE-LC phase transition (about 8 mN/m).

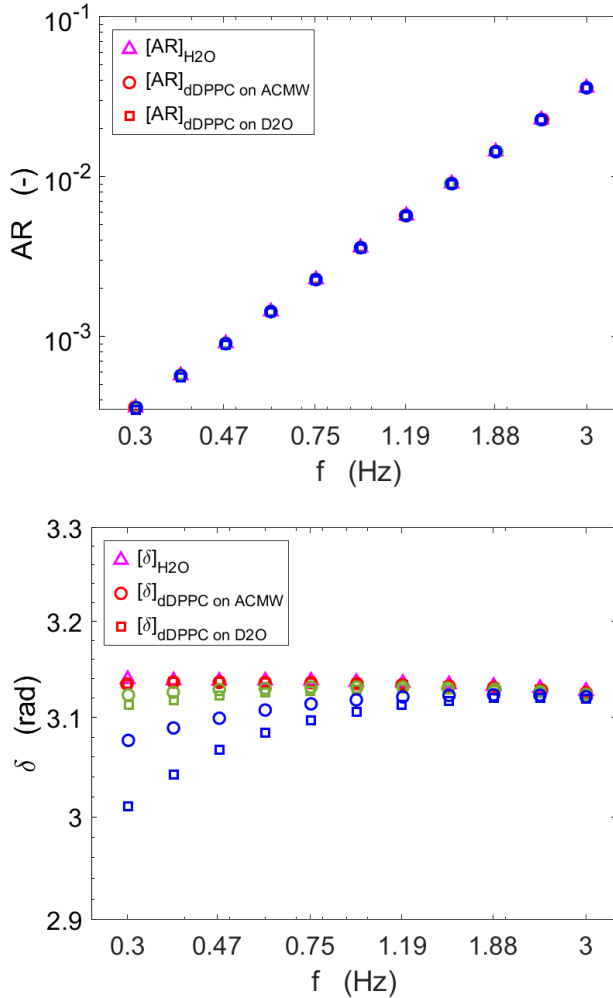


FIG. 4: $|AR^*|$ (panel A) and δ (panel B) as a function of frequency, at $\gamma_s = 3\%$. Circles: dDPPC monolayers onto ACMW subphase. Squares: dDPPC monolayers onto D2O subphase. Triangles: clean air/water interface. Red symbols: $\Pi = 25$ mN/m. Green symbols: $\Pi = 35$ mN/m. Blue symbols: $\Pi = 45$ mN/m.

Validation of the DWR ISR. In Figure 4 we show the dependency of the modulus of the complex amplitude ratio, $|AR^*|$, on the oscillation frequency for a clean air/water interface and the two measured contrast of DPPC monolayers at three different interfacial pressures: $\Pi = 25$ (red), 35 (green), and 45 (blue) mN/m. The mod-

ulus, $|AR^*|$, is similar in all of the interfaces, however the phase shift between the applied torque and the angular displacement shows differences. At 25 mN/m the measurements are practically indistinguishable respect to the clean interface and the same for high frequency measurements ($f \geq 2$ Hz) where the inertia contribution of the instrument to $|AR^*|$ is comparatively larger.

The calculated loss modulus, corresponding to the data shown in Figure 4 is shown on Figure 5 where two power law regimes can be conjectured with a crossover frequency that increases with the interfacial pressure. The storage modulus, G' is not shown because in the data presented here, the loss modulus is largely dominant; hence, the *loss tangent* is about 90° and the storage modulus can not be well characterized.

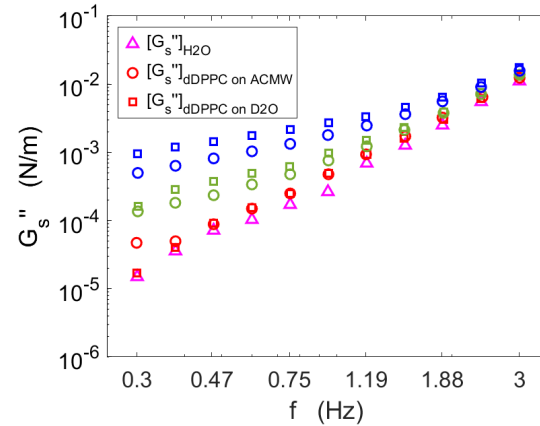


FIG. 5: Loss modulus, G'' , as a function of frequency, at $\gamma_s = 3\%$. Circles: dDPPC monolayers onto ACMW subphase. Squares: dDPPC monolayers onto D2O subphase. Triangles: apparent loss modulus for a clean air/water interface. Red symbols: $\Pi = 25$ mN/m. Green symbols: $\Pi = 30$ mN/m. Blue symbols: $\Pi = 35$ mN/m.

Several aspects of Figure 5 can be noticed: i) the loss modulus increases with the interfacial pressure, as expected, ii) the monolayers onto a D2O subphase show loss modulus values systematically slightly higher than the monolayers made on ACMW subphases, and iii) the *apparent* interfacial loss modulus obtained for the clean air/water interface indicates the resolution limit of the device in the experimental conditions here considered. The origin of this *apparent* interfacial loss modulus of the clean air/water interface can be traced back to the propagation of the uncertainties in the measurement of $|AR^*|$ and δ .

Validation of the neutron reflectometry measurements. A model considering two layers (DPPC head-group and aliphatic tails) and roughness has been employed by using ‘Lipid-Leaflet’ macro of *refnx* software that includes a molecular constraint ensuring the surface excess is the same in both layers. The data for the two isotropic contrasts were co-refined together under the assumption that the chemical structures are identical in

both cases. In Figure 6 an example of the reflectivity profiles for the two measured contrasts and the fitted SLD profiles across the vertical coordinates are represented in panels A and B, respectively. The values of the relevant parameters obtained through the fitting process are shown in Table I. The obtained reflectivity measurements are in good agreement with others previously obtained in FIGARO³⁶.

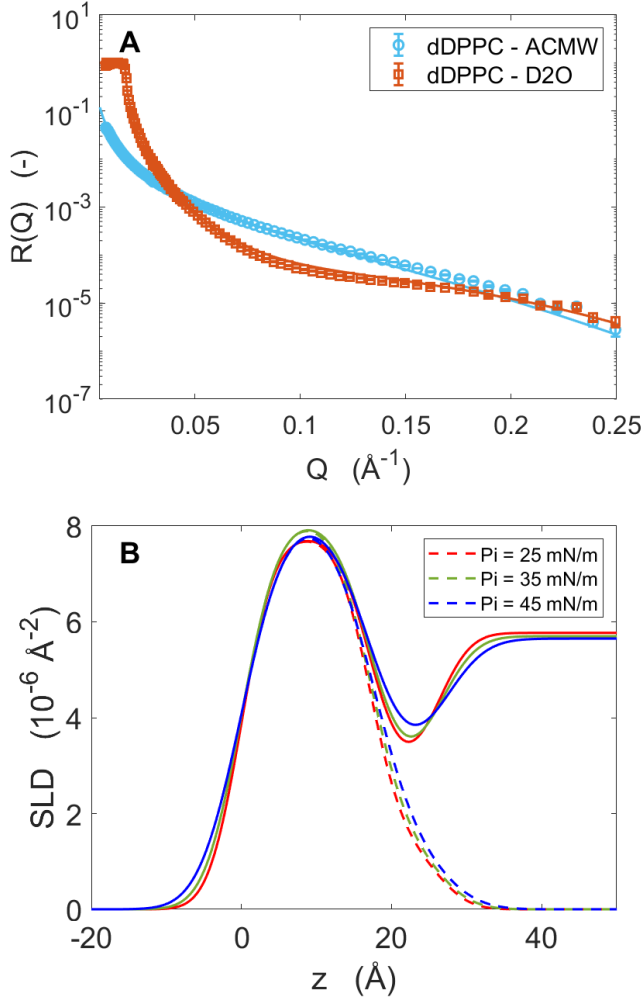


FIG. 6: Panel A: Reflectivity as a function of the scattering vector at $\Pi = 25$ mN/m for the two different subphases here used. Panel B: Fitted SLD profiles at $\Pi = 25$ mN/m (red lines), $\Pi = 35$ mN/m (green lines), and $\Pi = 45$ mN/m (blue lines) for the two different subphases (dashed lines: ACMW subphase; continuous lines: D2O subphase).

Finally, in Figure 7 we put together the information gained from the simultaneous interfacial rheology and neutron reflectometry measurements. In Figure 7, the values of the loss modulus (left axis), G'' , are represented by means of black symbols, and values of the area per molecule (right axis) are represented by red diamonds. All the measurements were taken at $f = 0.5$ Hz and $\gamma_s = 3$

%, at three interfacial pressure values. The circles pertain to dDPPC monolayers onto a ACMW subphase, and the squares to dDPPC monolayers onto a D2O subphase.

For pure DPPC monolayers an exponential relationship between the loss modulus and the interfacial pressure can be observed (see Figure 7). Measured values of dynamic moduli are in good agreement with other previous studies^{37,38}.

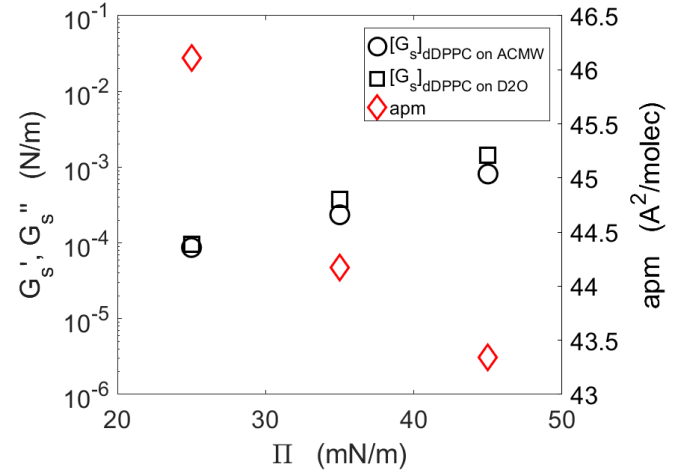


FIG. 7: Results of simultaneous measurements of the loss modulus (left axis; black symbols), G'' , and the area per molecule (right axis, red diamonds) at $f = 0.5$ Hz and $\gamma_s = 3$ %, at three interfacial pressure values. Circles: dDPPC monolayers onto ACMW subphase. Squares: dDPPC monolayers onto D2O subphase.

Moreover, the dependencies of the, simultaneously measured, loss modulus and the area per molecule, apm , are coherent with each other: the higher the interfacial pressure the higher are the dynamic moduli and the lower the mean area available for the surfactant molecules. This is expected since the higher the interfacial pressure, the more the molecules are compacted and their mobility is reduced.

IV. CONCLUSIONS

We describe a new sample environment setup that allows for *in-situ* measurements of neutron reflectivity and interfacial rheology on the same sample. The DWR geometry, coupled to a rotational rheometer, has been coupled to a Langmuir trough that fits on FIGARO anti-vibration table. An *ad-hoc* data acquisition program has been developed to obtain and analyze torque and angular position signals to calculate the interfacial dynamic moduli on-the-fly. Knowing the viscoelastic properties during the study of a fluid interface is of great interest to elucidate different phases and even characterize phase transitions. This setup is especially suitable for the study of kinetics and phase transitions as it allows the correlation of

TABLE I: Summary table with the fitted parameters at different interfacial pressures.

	Π (mN/m)	Chains thickness (\AA)	Headgroup thickness (\AA)	Area per molecule (\AA^2)
dDPPC	25	17.11 ± 0.03	9.00 ± 0.08	46.11 ± 0.02
	35	17.15 ± 0.02	9.00 ± 0.07	44.17 ± 0.02
	45	17.35 ± 0.02	9.00 ± 0.10	43.34 ± 0.02

thermodynamic, mechanical and structural parameters. In addition, it allows the saving of experiments, which is of great interest when dealing with particularly expensive or precious samples. A DPPC sample has served to validate the system and the results obtained agree well with others found in the literature for both neutron reflectometry and interfacial shear rheology.

ACKNOWLEDGEMENTS

The authors gratefully acknowledge the support of Simon Wood on mechanical design and fabrication. P.S.P. acknowledges the MICINN-ILL post-doc program for supporting his stay at ILL. J.T. and M.A.R. acknowledge the support of the Spanish Ministerio de Ciencia e Innovación (MCIN) - Agencia Estatal de Investigación (MCIN/AEI/10.13039/501100011033) through project PID2020-117080RB-C54. A.M. also acknowledges the financial support from MCIN/AEI under grant PID2021-129054NA-I00, from the Department of Education of the Basque Government under grant PIBA-2023-1-0054 and from the IKUR Strategy under the collaboration agreement between Ikerbasque Foundation and Materials Physics Center.

AUTHOR DECLARATIONS

Conflict of interest

The authors have no conflicts of interest to disclose.

- ¹G. G. Fuller and J. Vermant, “Complex fluid-fluid interfaces: Rheology and structure,” *Annual Review of Chemical and Biomolecular Engineering* **3**, 519–543 (2012).
- ²V. M. Kaganer, H. Möhwald, and P. Dutta, “Structure and phase transitions in langmuir monolayers,” *Rev. Mod. Phys.* **71**, 779–819 (1999).
- ³L. Braun, M. Uhlig, R. von Klitzing, and R. A. Campbell, “Polymers and surfactants at fluid interfaces studied with specular neutron reflectometry,” *Advances in Colloid and Interface Science* **247**, 130–148 (2017).
- ⁴J. Lu, R. Thomas, and J. Penfold, “Surfactant layers at the air/water interface: structure and composition,” *Advances in Colloid and Interface Science* **84**, 143–304 (2000).
- ⁵A. Maestro and P. Gutfreund, “In situ determination of the structure and composition of langmuir monolayers at the air/water interface by neutron and x-ray reflectivity and ellipsometry,” (2021).
- ⁶F. Gerber, M. P. Krafft, T. F. Vandamme, M. Goldmann, and P. Fontaine, “Fluidization of a dipalmitoyl phosphatidylcholine

monolayer by fluorocarbon gases: Potential use in lung surfactant therapy,” *Biophysical Journal* **90**, 3184–3192 (2006).

- ⁷J. Daillant and A. Gibaud, *X-ray and Neutron Reflectivity: Principles and Applications*, Vol. 58 (Springer Berlin Heidelberg, 1999).
- ⁸M. P. Krafft, F. Giulieri, P. Fontaine, and M. Goldmann, “Reversible stepwise formation of mono- and bilayers of a fluorocarbon/hydrocarbon diblock on top of a phospholipid langmuir monolayer. a case of vertical phase separation,” *Langmuir* **17**, 6577–6584 (2001).
- ⁹J. F. Gonzalez-Martinez, E. Kakar, S. Erkselius, N. Rehnberg, and J. Sotres, “Effect of relative humidity on the viscoelasticity of thin organic films studied by contact thermal noise afm,” *Langmuir* **35**, 6015–6023 (2019).
- ¹⁰J. F. Gonzalez-Martinez, E. Kakar, S. Erkselius, N. Rehnberg, and J. Sotres, “The role of cross-linking in the scratch resistance of organic coatings: An investigation using atomic force microscopy,” *Wear* **418–419**, 151–159 (2019).
- ¹¹P. Nestler and C. A. Helm, “Determination of refractive index and layer thickness of nm-thin films via ellipsometry,” *Opt. Express* **25**, 27077–27085 (2017).
- ¹²D. Ducharme, A. Tessier, and S. C. Russev, “Simultaneous thickness and refractive index determination of monolayers deposited on an aqueous subphase by null ellipsometry,” *Langmuir* **17**, 7529–7534 (2001).
- ¹³H. R. Vutukuri, M. Hoore, C. Abaurrea-Velasco, L. van Buren, A. Dutto, T. Auth, D. A. Fedosov, G. Gompper, and J. Vermant, “Active particles induce large shape deformations in giant lipid vesicles,” *Nature* **586**, 52–56 (2020).
- ¹⁴P. J. Beltramo and J. Vermant, “Simple optical imaging of nanoscale features in free-standing films,” *ACS Omega* **1**, 363–370 (2016).
- ¹⁵S. Rivière, S. Hénon, J. Meunier, D. K. Schwartz, M. Tsao, and C. M. Knobler, “Textures and phase transitions in langmuir monolayers of fatty acids. a comparative brewster angle microscope and polarized fluorescence microscope study,” *The Journal of Chemical Physics* **101**, 10045–10051 (1994).
- ¹⁶J. Carrascosa-Tejedor, A. Santamaria, A. Tummino, I. Varga, M. Efstratiou, M. J. Lawrence, A. Maestro, and R. A. Campbell, “Polyelectrolyte/surfactant films: from 2d to 3d structural control,” *Chemical Communications* **58**, 10687–10690 (2022).
- ¹⁷J. Carrascosa-Tejedor, L. M. Miñarro, M. Efstratiou, I. Varga, M. W. A. Skoda, P. Gutfreund, A. Maestro, M. J. Lawrence, and R. A. Campbell, “Control of the structure and morphology of polypeptide/surfactant spread films by exploiting specific interactions,” *Nanoscale* **15**, 11141–11154 (2023).
- ¹⁸C. F. Brooks, G. G. Fuller, C. W. Frank, and C. R. Robertson, “Interfacial stress rheometer to study rheological transitions in monolayers at the air-water interface,” *Langmuir* **15**, 2450–2459 (1999).
- ¹⁹J. Tajuelo, J. M. Pastor, F. Martínez-Pedrero, M. Vázquez, F. Ortega, R. G. Rubio, and M. A. Rubio, “Magnetic microwire probes for the magnetic rod interfacial stress rheometer,” *Langmuir* **31**, 1410–1420 (2015).
- ²⁰J. Tajuelo, J. M. Pastor, and M. A. Rubio, “A magnetic rod interfacial shear rheometer driven by a mobile magnetic trap,” *Journal of Rheology* **60**, 1095–1113 (2016).
- ²¹Z. A. Zell, V. Mansard, J. Wright, K. Kim, S. Q. Choi, and T. M. Squires, “Linear and nonlinear microrheometry of small

- samples and interfaces using microfabricated probes,” *Journal of Rheology* **60**, 141–159 (2016).
- ²²P. Erni, P. Fischer, E. J. Windhab, V. Kusnezov, H. Stettin, and J. Lauger, “Stress- and strain-controlled measurements of interfacial shear viscosity and viscoelasticity at liquid/liquid and gas/liquid interfaces,” *Review of Scientific Instruments* **74**, 4916–4924 (2003).
- ²³J. Tajuelo, M. A. Rubio, and J. M. Pastor, “Flow field based data processing for the oscillating conical bob interfacial shear rheometer,” *Journal of Rheology* **62**, 295–311 (2017).
- ²⁴P. Sanchez-Puga, J. Tajuelo, J. M. Pastor, and M. A. Rubio, “Biconedrag—a data processing application for the oscillating conical bob interfacial shear rheometer,” *Computer Physics Communications* **239**, 184–196 (2019).
- ²⁵S. Vandebril, A. Franck, G. G. Fuller, P. Moldenaers, and J. Vermant, “A double wall-ring geometry for interfacial shear rheometry,” *Rheologica Acta* **49**, 131–144 (2010).
- ²⁶S. Reynaert, C. F. Brooks, P. Moldenaers, J. Vermant, and G. G. Fuller, “Analysis of the magnetic rod interfacial stress rheometer,” *Journal of Rheology* **52**, 261–285 (2008).
- ²⁷T. Verwijlen, P. Moldenaers, H. A. Stone, and J. Vermant, “Study of the flow field in the magnetic rod interfacial stress rheometer,” *Langmuir* **27**, 9345–9358 (2011), pMID: 21696160.
- ²⁸P. Sanchez-Puga, J. Tajuelo, J. M. Pastor, and M. A. Rubio, “Flow field-based data analysis in interfacial shear rheometry,” *Advances in Colloid and Interface Science* **288**, 102332 (2021).
- ²⁹R. A. Campbell, H. P. Wacklin, I. Sutton, R. Cubitt, and G. Fragneto, “Figaro: The new horizontal neutron reflectometer at the ill,” *The European Physical Journal Plus* **126**, 107 (2011).
- ³⁰P. Sanchez-Puga and M. A. Rubio, “Dwr-drag: A new generation software for the double wall-ring interfacial shear rheometer’s data analysis,” (2024), arXiv:2408.15755 [cond-mat.soft].
- ³¹R. A. Campbell, “Recent advances in resolving kinetic and dynamic processes at the air/water interface using specular neutron reflectometry,” *Current Opinion in Colloid and Interface Science* **37**, 49–60 (2018).
- ³²P. Gutfreund, T. Saerbeck, M. A. Gonzalez, E. Pellegrini, M. Laver, C. Dewhurst, and R. Cubitt, “Towards generalized data reduction on a chopper-based time-of-flight neutron reflectometer,” *Journal of Applied Crystallography* **51**, 606–615 (2018).
- ³³D. A. Edwards, H. Brenner, D. T. Wasan, and A. M. Kraynik, *Interfacial Transport Processes and Rheology*, edited by Butterworth-Heinemann (Butterworth-Heinemann, 1991) p. 576.
- ³⁴A. R. J. Nelson and S. W. Prescott, “refnx : neutron and x-ray reflectometry analysis in python,” *Journal of Applied Crystallography* **52**, 193–200 (2019).
- ³⁵Y. Gerelli, “Aurore: new software for neutron reflectivity data analysis,” *Journal of Applied Crystallography* **49**, 330–339 (2016).
- ³⁶R. A. Campbell, Y. Saaka, Y. Shao, Y. Gerelli, R. Cubitt, E. Nazaruk, D. Matyszewska, and M. J. Lawrence, “Structure of surfactant and phospholipid monolayers at the air/water interface modeled from neutron reflectivity data,” *Journal of Colloid and Interface Science* **531**, 98–108 (2018).
- ³⁷K. Kim, S. Q. Choi, J. A. Zasadzinski, and T. M. Squires, “Interfacial microrheology of dppc monolayers at the air–water interface,” *Soft Matter* **7**, 7782 (2011).
- ³⁸E. Hermans and J. Vermant, “Interfacial shear rheology of dppc under physiologically relevant conditions,” *Soft Matter* **10**, 175–186 (2014).